Original Article

Institution of MECHANICAL ENGINEERS
Journal of ENGINEERING MANUFACTURE

Proc IMechE Part B:
J Engineering Manufacture
0(0) 1–14

DOI: 10.1177/0954405413510291
pib.sagepub.com
SAGE

Effects of machining parameters and tool geometry on serrated chip formation, specific forces and energies in orthogonal cutting of nickel-based super alloy Inconel 100

Tuğrul Özel and Durul Ulutan

Abstract

Nickel-based alloys are widely used in applications requiring high strength at elevated temperatures such as in aircraft jet engines. However, nickel-based alloys such as Inconel 100 are still considered difficult-to-machine metal alloys. In this study, specially designed orthogonal cutting tests on Inconel 100 nickel-based alloy have been conducted using WC/Co cutting tool with two varying rake angles, cutting edge radii and at wide ranges of cutting speed and feed. Effects of those parameters on specific forces have been investigated. Serrated and segmented chip formation is observed and the mechanics of segmented chip have been modeled and validated using the experimental test data. Chip microscopic images are utilized in measuring and calculating chip formation angles, shear strain, and shear strain rate in the main shear zone and within the shear bands. It was found that segmentation is highly influenced by machining conditions, and energy distributions calculated with regard to machining parameters reveal that friction dissipation and material separation are significant in machining of Inconel 100 nickel-based alloy.

Keywords

Nickel-based super alloy, tool edge radius, segmented chip formation, specific forces, friction

Date received: 19 April 2013; accepted: 3 October 2013

Introduction

Nickel-based alloys are often used in applications requiring superior strength in high temperatures and exist mainly as in Ni-Co-Cr, Ni-Fe-Cr, or Ni-Co-Fe alloying forms. In general, these alloys can withstand high temperatures without losing their strength. Therefore, they are a good choice for applications requiring high strength at very high temperatures such as hot sections of aircraft and gas engines. They often can be obtained via certain manufacturing routes such as forging, casting, or powder compaction followed by sintering. Particularly, Inconel 100 (IN-100) nickel-based alloy can be obtained through casting or sintering. In all these cases, the parts must be processed via finish material removal processes. However, machinability of these alloys is considered highly difficult[1–3] due to their abundant fracture toughness and strain hardening behavior.[4–6] Workpiece subsurface forms a hardened layer due to machining-induced thermal–mechanical loading.[7] Furthermore, heat generated during machining cannot be rapidly dissipated due to low thermal conductivity and this leads to excessive tool wear.[8,9] At high temperatures, nickel-based alloy tends to adhere to the cutting tool edge and alloying related hard particles act as abrasives creating further complications of excessive wear.[3,9–11] In the literature, extensive number of research studies has been reported addressing the issues related to machining nickel-based alloys.

In order to improve machinability and tool life, tool materials such as uncoated and coated carbides and ceramics have been widely used.[1–16] It was found that

Manufacturing & Automation Research Laboratory, Department of Industrial and Systems Engineering, Rutgers University, Piscataway, NJ, USA

Corresponding author:
Tuğrul Özel, Manufacturing & Automation Research Laboratory, Department of Industrial and Systems Engineering, Rutgers University, Piscataway, NJ 08854, USA.
Email: ozel@rutgers.edu

tool edge radius is more critical since the cutting edge geometry cannot be perfectly sharp and must have a finite edge radius in these tool materials with high hardness but relatively low toughness. Then, tool edge induces large strains on the workpiece during cutting; hence, a hard layer forms on the subsurface resulting from plowing. While a positive rake tool geometry decreases plowing by shearing away the chip from workpiece efficiently and minimizes not only build-up on the cutting edge but also work hardening layer formation on the workpiece.

For rouging operations, a large edge radius is recommended to increase the strength of the cutting edge and reduce chipping. Since a larger edge radius tool induces larger strains and greater subsurface damage, work hardened layer would be thicker on the machined surface. The thickness of the work hardened layer is usually 0.05–0.075 mm and can be as large as 0.125 mm. Hence, a depth of cut deeper than the thickness of the work hardened layer must be taken in sequential cuts. In both semi-finishing and finishing operations, a positive rake cutting edge is recommended.

In addition, tool edge geometry and rake angle are found to be highly influential where especially tool edge geometry affects material adhesion and surface finish in machining of nickel-based super alloys.[15] In general, very small edge radius insert edges are preferred to minimize material adhesion and improve surface finish during machining. However, the effect of tool edge geometry and rake angle to a fuller extent still yet to be revealed on specific cutting, material separation, and friction energies with resultant fracture toughness of nickel-based alloys for process planning purposes.

In machining Inconel 718 (IN-718), high degrees of the work hardening with a rich layer of plastic deformation have been observed.[15] Material hardening behavior is claimed to be affected by the size of the grains, which was changing mainly due to dynamic recovery, refinement, and precipitation.[17] In machining of UDIMET 720, it was observed that the microhardness of the material was decreasing from the surface into the depth direction significantly within the cutting-affected layer.[14]

In machining powder compaction sintered nickel-based alloy RR_X (which is considered similar to Inconel), it was observed that the processed chips adhere and redeposit on the machined surfaces during rough and finish turning.[12] However, changing depth of cut values in each turning pass has been seen effective in minimizing the occurrence of redeposition.

Characteristically, most nickel-based alloys include some content of carbide particles as gamma prime phase (γ') in their structure. Carbide cutting tool materials include tungsten carbide grains in cobalt matrix. During finish machining, these carbide particles irregularly dislodge from the workpiece or tool structure and deposit onto the workpiece surface causing sudden rise in shear stress and leading to serious surface defects at the locations where product's fatigue performance

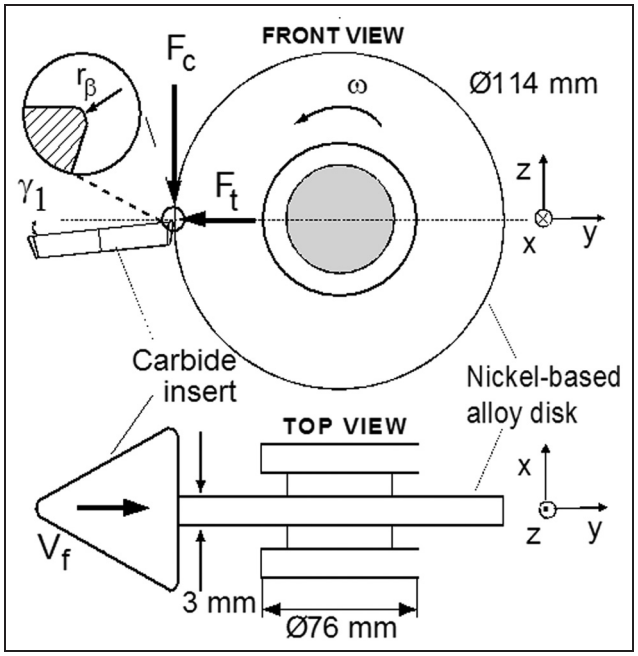

Figure 1. Orthogonal cutting of a nickel-based super alloy workpiece specimens.

decreases substantially.[18,19,20] The degree of carbide cracking also depends on the tool edge radius and cutting conditions especially depth of cut since at low feeds and depth of cuts, machining process is more sensitive to carbide particles that are typically in the size of 20 μm.

Consequently, there is a need for additional experimental studies and analyses to fully understand the influence of tool geometry and edge radius in machining of nickel-based alloys. Therefore, experimental investigations and related analyses are carried out in this study to understand the effects of machining parameters such as cutting speed and feed and tool geometry such as rake angle and edge radius on process mechanics, namely, segmented chip formation, specific energies for shearing, friction and material separation, and friction coefficient between carbide tool and the workpiece in machining of Inconel 100 (IN-100 nickel-based super alloy.

Experimental study

Orthogonal turning of webs (3 mm thick) has been performed using uncoated tungsten carbide (WC) cutting tools in a rigid CNC turning center (ROMI Centur 35E) at Manufacturing & Automation Research Laboratory of Rutgers University. Test workpiece is machined with plunge turning. This experimental setup has created the orthogonal cutting condition, as illustrated in Figure 1. On nickel-based alloy disks, grooves (19 mm deep and 3 mm wide) are machined at a cutting speed (v_c) of 18 m/min and a feed (h) of 0.06 mm/rev to create the test workpiece with multiple webs. The

cutting forces were measured with a Kistler turret-type three-component force dynamometer (Type 9121, Kistler Instruments AG, Switzerland) and high-speed data acquisition devices. The signal generated at each component at the force dynamometer was amplified using charge amplifiers (Kistler Type 5814B1, Kistler Instruments AG, Switzerland). The amplified signal is acquired and sampled (a sampling frequency of 1000 Hz per channel) using a laptop computer-based data acquisition system (PCMCIA card and Type 2825A-02-1; Kistler DynoWare software).

The experiments have been conducted using uncoated carbide tools with two different edge radiuses (r_β = 10 and 25 μm) and tool holders with 0° and +3° rake angles (γ_1) at four different cutting speeds (v_c = 6, 12, 18, and 24 m/min) and six different feeds or uncut chip thicknesses (h = 0.01, 0.025, 0.05, 0.075, 0.1, and 0.125 mm/rev).

Analysis of chip morphology

The influence of serrated chip formation on machining process outputs—cutting forces, temperature and surface roughness and integrity—is profound. Therefore, a thorough understanding of mechanics of serrated chip formation in nickel-based super alloy machining is considered important.

Fundamental mechanism of serrated chip formation in titanium alloys (e.g. Ti-6Al-4V) and nickel-based alloys (e.g. IN-718) has been long debated. According to one theory,[3] this is due to the thermal softening (i.e. localized shearing). Another theory claims that there exists a crack initiation in the primary shearing zone (i.e. a narrow band between the tool tip and the chip free surface), which causes serration in the chips.[4–7]

Both theories are supported by experimental evidences, and the common belief is that both mechanisms are in effect. At low cutting speeds, a crack-initiated serration occurs, and at high cutting speeds, localized shearing-based serration occurs due to higher temperatures and it becomes more dominant.

In the orthogonal cutting of nickel-based super alloy IN-100, morphology of the chip formation has been investigated. Chip images captured using field emission scanning electron microscopy (FESEM) depict highly serrated shape with regions of high plastic deformations (adiabatic shear bands) and cracks mixed, as shown in Figure 2. It should be noted that views of segmented chips were accurate enough to reveal the chip segmentation dimensions and in close-up examination lamellar shear zones.

It is believed that adiabatic shear band is a form of failure mechanism that occurs in both titanium and nickel-based super alloys when they are deformed at a high rate in machining processes. Adiabatic shear bands are usually very narrow, typically 5–50 μm, and they consist of very highly sheared material. It should be noted that "adiabatic" is a thermodynamic term meaning an absence of heat transfer—the heat produced is

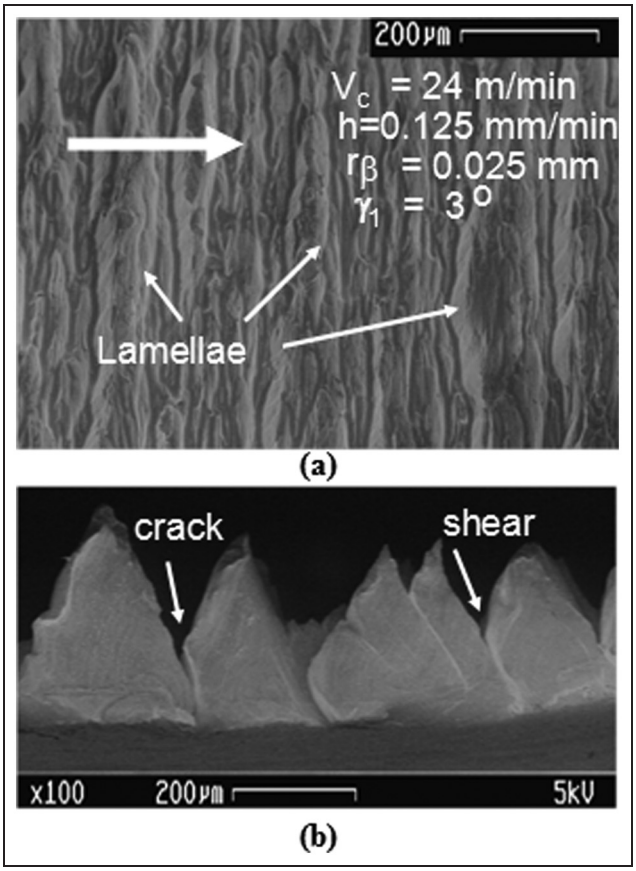

Figure 2. Morphology of the continuous but segmented chips: (a) lamellae on the free surface of the chip and (b) cross-sectional image of the same chip with shear and crack formation.

retained in the zone where it is created. Furthermore, adiabatic shear bands are commonly the precursors to fracture.

The presence of adiabatic shear bands in serrated chips does not rule out the existence of segmented chip formation with crack initiation. Many experimental observations of chip morphology indicated that both cracks and adiabatic shear bands can coexist.[21–26]

In general, continuous but serrated chip formation has been observed with the cutting conditions specified in this study (see Figure 3). At lower feeds, continuous chips with little or no serration were seen. Segmentation increased at higher feeds and cutting speeds similar to other observations reported for titanium and nickel-based alloys in the literature.[16,25,27] Segmentation has been more dominantly affected by the increase in feed or uncut chip thickness increase.

Chip FESEM images revealed brighter coloration occurred at higher cutting speeds indicating temperature rise–related material microstructure alteration. This alternation may be an indication in change in crystalline structure due to the cutting-related temperature rise that can reach above dynamic recrystallization of nickel-based alloy. During the machining operation, the workpiece material is exposed to a thermal, mechanical, and chemical energy that can lead to strain aging and recrystallization of the material.[21,22,24] Due to the strain

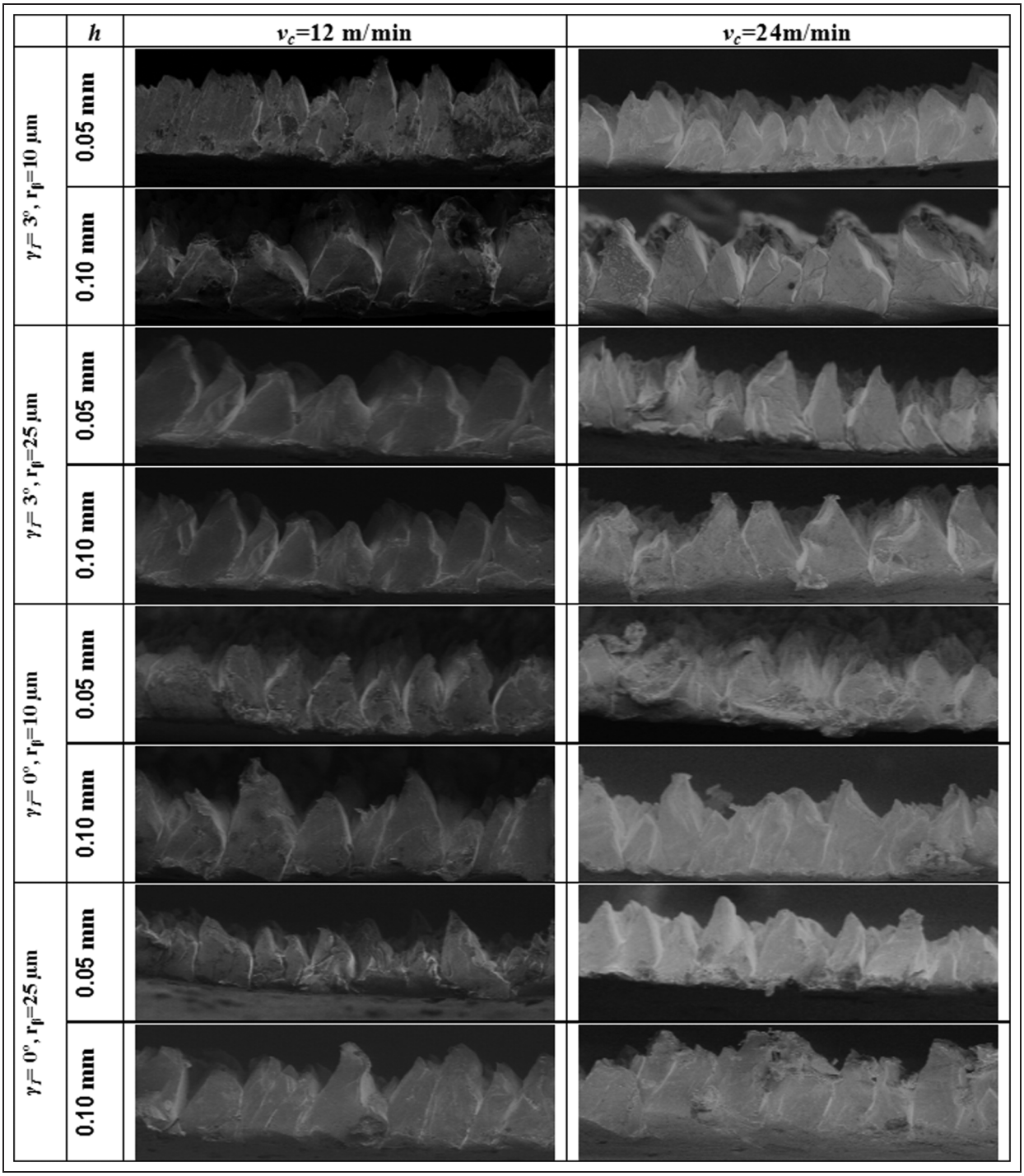

Figure 3. FESEM images of segmented chip formation.

aging process, the material might become harder but less ductile, and recrystallization might cause the material to become less hard but more ductile. It is believed that these microstructural alterations can lead to white layer formation when strain aging is dominant, and when recrystallization is also observed.[23,24,26]

Mechanics of serrated chip formation

Many researchers investigated the mechanics and dynamics of chip formation when machining heat resistant alloys such as titanium and nickel-based alloys.[21–23,25] Most recently, Cotterell and Byrne[27] have investigated the dynamics of chip formation and the relation between cutting parameters and chip serration in Ti-6Al-4V alloy. Pawade et al.[16] investigated the specific shear energy of the workpiece material in machining IN-718 using an elastic–viscoplastic analytical model they created and found out that shear band spacing increases with increasing feed. Fang et al.[28] provided a segmented chip formation model and investigated chip formation mechanics in machining of

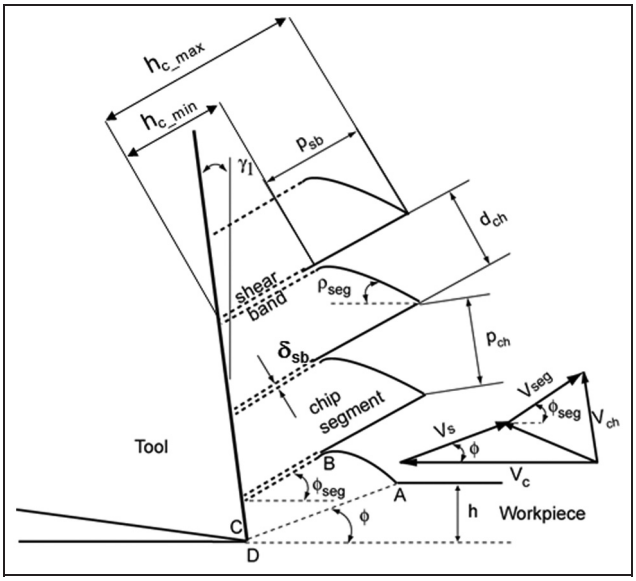

Figure 4. Serrated chip formation model and its hodograph.

aluminum alloys. In this study, we utilized a segmented chip formation model that is similar to models presented by Cotterell and Byrne,[27] Pawade et al.,[16] and Fang et al.[28]

In this model, the serration of the chip creates a sawtooth shape, and the pitch of these chips (p_{ch}) and the shear band thickness (δ_{sb}) parameters become important factors in determining the shear strain at the adiabatic shear band. Also, the chip morphology will have peaks and valleys, which makes the measurement of the chip thickness more difficult. Instead, the minimum chip thickness of a sample and a maximum chip thickness are measured, and the arithmetic average of these two is accepted to be the experimental chip thickness. According to this model, average shear strain calculation can be done as follows.[27]

An important measure of chip formation mechanism in nickel-based alloy machining, which is related to adiabatic shearing and crack formation, is the degree of segmentation. It also indicates the severity of chip segmentation. The degree of segmentation (D_s) is formulated using the minimum (h_{c_min}) and maximum (h_{c_max}) experimental chip thicknesses along the serrated chips where their locations are indicated in Figure 4[28]

$$D_s = \frac{h_{c\_max} - h_{c\_min}}{h_{c\_\max}} \tag{1}$$

The chip ratio (r_c) is defined by the ratio of undeformed chip thickness (h) (or feed in orthogonal cutting) to the average thickness of the segmented chips (h_c) that are measured experimentally

$$r_c = \frac{h}{h_c} \tag{2}$$

Hence, the shear angle can be found utilizing the measured chip ratios using the following formula,

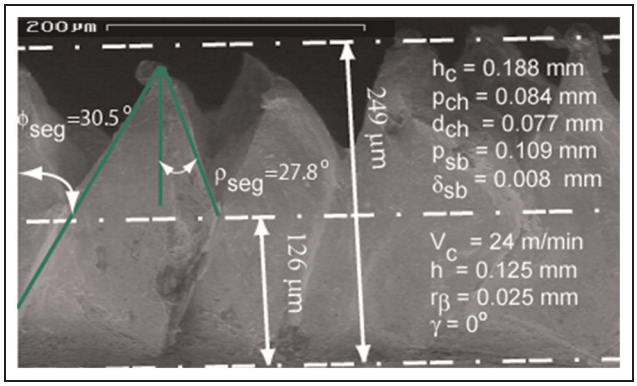

Figure 5. An example for the chip morphology measurements.

which is derived from the ratio (r_c) of undeformed chip thickness (h) to the average chip thickness (h_c) and rake angle (γ_1)

$$\phi = atan\left(\frac{r_c cos(\gamma_1)}{1 - r_c sin(\gamma_1)}\right) \tag{3}$$

Following this formulation, the shear strain in the primary shear zone (γ) can be found and the calculation based on continuous chip formation assumption becomes

$$\gamma = \frac{cos(\gamma_1)}{sin(\phi)cos(\phi - \gamma_1)} \tag{4}$$

In addition, average shear strain in segmented chip (γ_{seg}), average shear strain in the shear bands (γ_{sb}), and average strain rate based on segmented chip calculations become as suggested in Cotterell and Byrne[27]

$$\gamma_{seg} = \frac{sin(\rho_{seg})}{sin(\phi_{seg})sin(\phi_{seg} + \rho_{seg})} \tag{5}$$

$$\gamma_{sb} = \gamma_{seg} + \frac{p_{sb}}{\delta_{sb}} \tag{6}$$

$$\dot{\gamma} = \frac{cos(\gamma_1)}{sin(\phi - \gamma_1)}\frac{v_c}{\delta_{sb}} \tag{7}$$

where ρ_{seg} is chip segment angle, φ_{seg} is shear angle at the chip segment, p_{sb} is depth of segmentation, and δ_{sb} is shear band thickness. Then, using FESEM images and measurements on chip morphology (see Figure 5), average strain and strain rate can be found (Table 1).

It should be noted that severe shearing (between 10 and 30 mm/mm) occurs within the shear bands. This severity of deformations can also be seen as potential for fracture strain–initiated crack formation and indicates possible crack initiation on the machined surface.

Effects of machining conditions on degree of segmentation

The overall effects of machining conditions on degree of segmentation are shown in Figure 6. It is observed

Table 1. Influence of machining and tool geometry parameters on calculated strain and strain rates.

		v_c (m/min)	h (mm)	γ	γ_{seg}	γ_{sb}	$\dot{\gamma}$ (1/s)
$\gamma = 0°$	r_β = 10 μm	12	0.075	2.05	1.76	10.76	80,430
		12	0.100	2.16	1.57	25.17	71,945
		12	0.125	2.26	1.50	14.75	48,277
		24	0.075	2.63	1.09	10.37	136,360
		24	0.100	2.42	1.59	21.92	94,837
		24	0.125	2.30	1.15	30.31	132,869
	r_β = 25 μm	12	0.075	2.18	1.26	12.01	45,486
		12	0.100	2.24	1.10	13.21	42,306
		12	0.125	2.00	1.59	37.59	141,704
		24	0.075	2.40	1.90	14.70	168,942
		24	0.100	2.17	1.85	18.65	144,222
		24	0.125	2.17	1.08	14.71	90,139
$\gamma = 3°$	r_β = 10 μm	12	0.075	2.15	2.19	34.69	204,891
		12	0.100	1.92	1.74	16.49	79,433
		12	0.125	1.94	1.75	34.95	65,574
		24	0.075	2.24	0.83	–	–
		24	0.100	2.71	1.61	28.04	166,393
		24	0.125	2.13	0.83	29.03	161,224
	r_β = 25 μm	12	0.075	2.55	1.31	16.65	88,759
		12	0.100	1.99	2.03	12.20	58,841
		12	0.125	2.05	1.05	15.05	62,667
		24	0.075	2.04	1.49	21.16	249,258
		24	0.100	1.95	1.36	11.93	96,158
		24	0.125	1.92	0.99	24.24	79,631

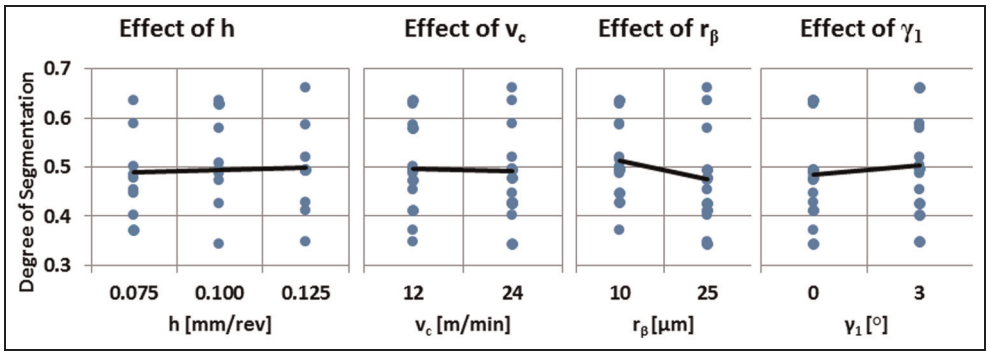

Figure 6. Effects of feed (h), cutting speed (v_c), edge radius (r_β), and rake angle (γ_1) on the degree of segmentation.

that increasing feed (h) or cutting speed (v_c) does not have a significant effect on the degree of segmentation (D_s) (<5%), whereas increasing cutting edge radius (r_β) (~5%) and decreasing rake angle (γ_1) (~10%) decrease the degree of segmentation.

Effects of machining conditions on main shear angle

The effects of machining conditions on the main shear angle (φ) are given in Figure 7. While all the parameters had notable effects on the main shear angle, it can be observed that with increasing feed (h) and decreasing cutting speed (v_c), the shear angle increased significantly (~20%). With increasing cutting edge radius (r_β) and rake angle (γ_1), a less significant increase (~10%) in the shear angle was also observed.

Effects of machining conditions on segmented shear angle

The effects of machining conditions on segmented shear angle, φ_{seg} (see Figure 4), are given in Figure 8. While changing cutting edge radius (r_β) and rake angle (γ_1) did not have significant effects (<5%), it was observed that with increasing feed (h) and cutting speed (v_c), the segmented shear angle increased by 10%−20%.

Effects of machining conditions on chip segment angle

The effects of machining conditions on chip segment angle (ρ_{seg}, see Figure 4) are given in Figure 9. With increasing cutting speed (v_c), a ~25% decrease in the

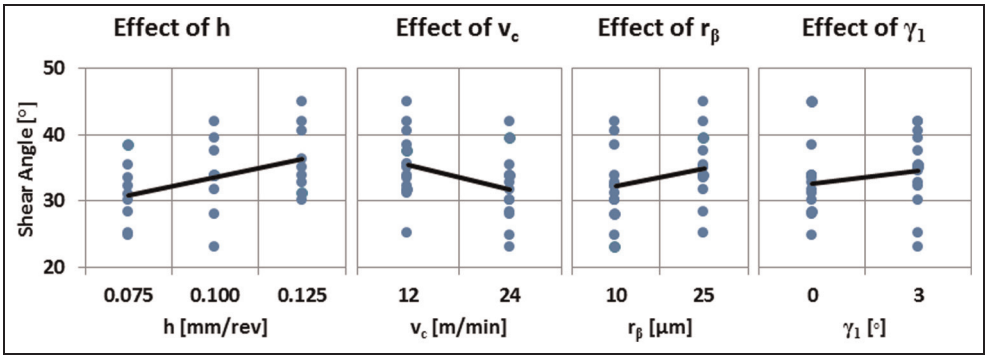

Figure 7. Effects of feed (h), cutting speed (v_c), edge radius (r_β), and rake angle (γ_1) on shear angle.

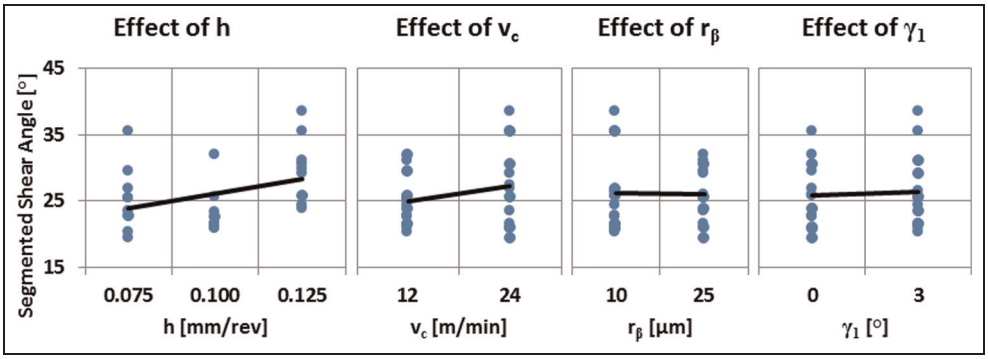

Figure 8. Effects of feed (h), cutting speed (v_c), edge radius (r_β), and rake angle (γ_1) on segmented shear angle.

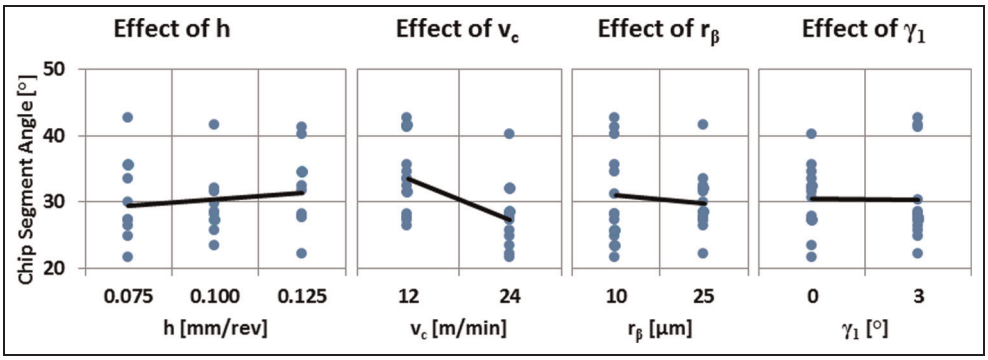

Figure 9. Effects of feed (h), cutting speed (v_c), edge radius (r_β), and rake angle (γ_1) on chip segment angle.

chip segment angle was observed. In addition, increasing feed (h) increased the chip segment angle by ~7%. The other parameters did not have significant effects on the chip segment angle (<5%).

Effects of machining conditions on shear strain in shear band

The shear strain in the shear band (γ_{sb}, see Figure 4) has been found to be in the range of 10–40, indicating a very rapid secondary shearing due to work material yielding and perhaps flow softening or dynamic recrystallization-related weakening. The effects of machining conditions on shear strain in shear band indicate an increase when feed (h) and rake angle (γ_1) are increased (~46% and ~32%), and cutting edge radius (r_β) is decreased (~16%), as shown in Figure 10. Cutting speed (v_c) did not have an observable effect on the shear strain in shear band (<1%).

Effects of machining conditions on shear strain rate

As well known, increased cutting speed increases the shear strain rate in the cutting zone. The results shown in Figure 11 agree with this common knowledge, indicating a ~40% increase in shear strain rate with increasing cutting speed (v_c). The effects of other machining conditions such as edge radius (r_β), rake

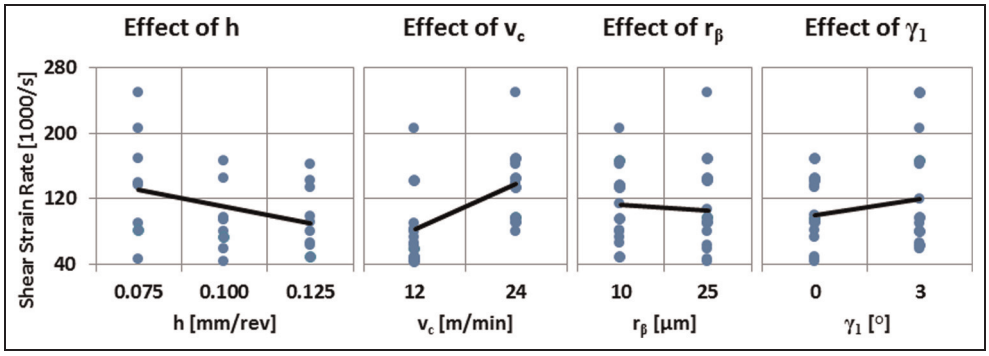

Figure 10. Effects of feed (h), cutting speed (v_c), edge radius (r_β), and rake angle (γ_1) on shear strain in shear band.

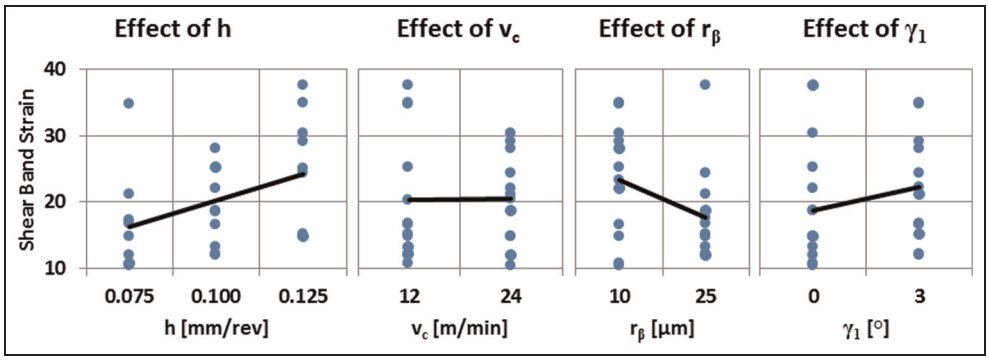

Figure 11. Effects of feed (h), cutting speed (v_c), edge radius (r_β), and rake angle (γ_1) on shear strain rate.

angle (γ_1), and feed (h) on shear strain rate are also given in Figure 11. Increased feed (h) caused a decrease of ~30% in shear strain rate. In addition, a neutral rake angle of ($\gamma_1 = 0°$) resulted in lower shear strain rate (~16%), and a smaller edge radius (r_β) resulted in higher shear strain rate (~7%).

Specific cutting forces and energy distributions

As widely reported in the literature, machining nickel-based alloys often results in extremely high specific cutting forces. The highest forces are encountered at lower cutting speeds and feeds. The main reason for this observation is the increasing specific energy for shearing and the material separation as suggested by Atkins[29] and Subbiah and Melkote,[30] even though this approach has been criticized by some researchers.

Therefore, in order to better understand the effects of tool edge radius, rake angle and cutting speed on machinability, specific forces and energies for shearing, friction, and material separation are investigated. Specific cutting forces measured in orthogonal cutting tests of nickel-based alloy disks have been presented in Figure 12. Positive rake angle and larger edge radius resulted in higher specific cutting forces. At higher cutting speeds, specific cutting force decreases due to thermal softening and strain softening at higher strain rates.

In machining processes, the temperature increase during operation is mainly caused by three different energy sources: shear energy (plastic dissipation), frictional dissipation, and surface formation (material separation). The total cutting energy $F_c v_c$ is the sum of these three components, since the cutting force and velocity are the sources for these energy terms

$$F_c v_c = (\tau_y \gamma)(hwv_c) + [F_c \, sec(\beta - \gamma_1) sin(\beta)] \frac{v_c \, sin(\phi)}{cos(\phi - \gamma_1)} + Rwv_c \tag{8}$$

In this equation, F_c is the cutting force; v_c is the cutting velocity; τ_y is the shear yield stress; γ is the shear strain; h is the uncut chip thickness; w is the width of cut; β, γ_1, and φ are the friction, rake, and shear angles, respectively; and R is the fracture toughness of the material.[29] This equation can also be written as

$$F_c = \left(\frac{\tau_y \gamma w}{Q}\right) h + \frac{Rw}{Q} \tag{9}$$

Here, Q is a common denominator represented by

$$Q = 1 - \frac{sin(\beta) sin(\phi)}{cos(\beta - \gamma_1) cos(\phi - \gamma_1)} \tag{10}$$

In order to find the fracture toughness (R) and the shear yield stress (τ_y) of the material, we follow a procedure suggested by Atkins[31] and also outlined in

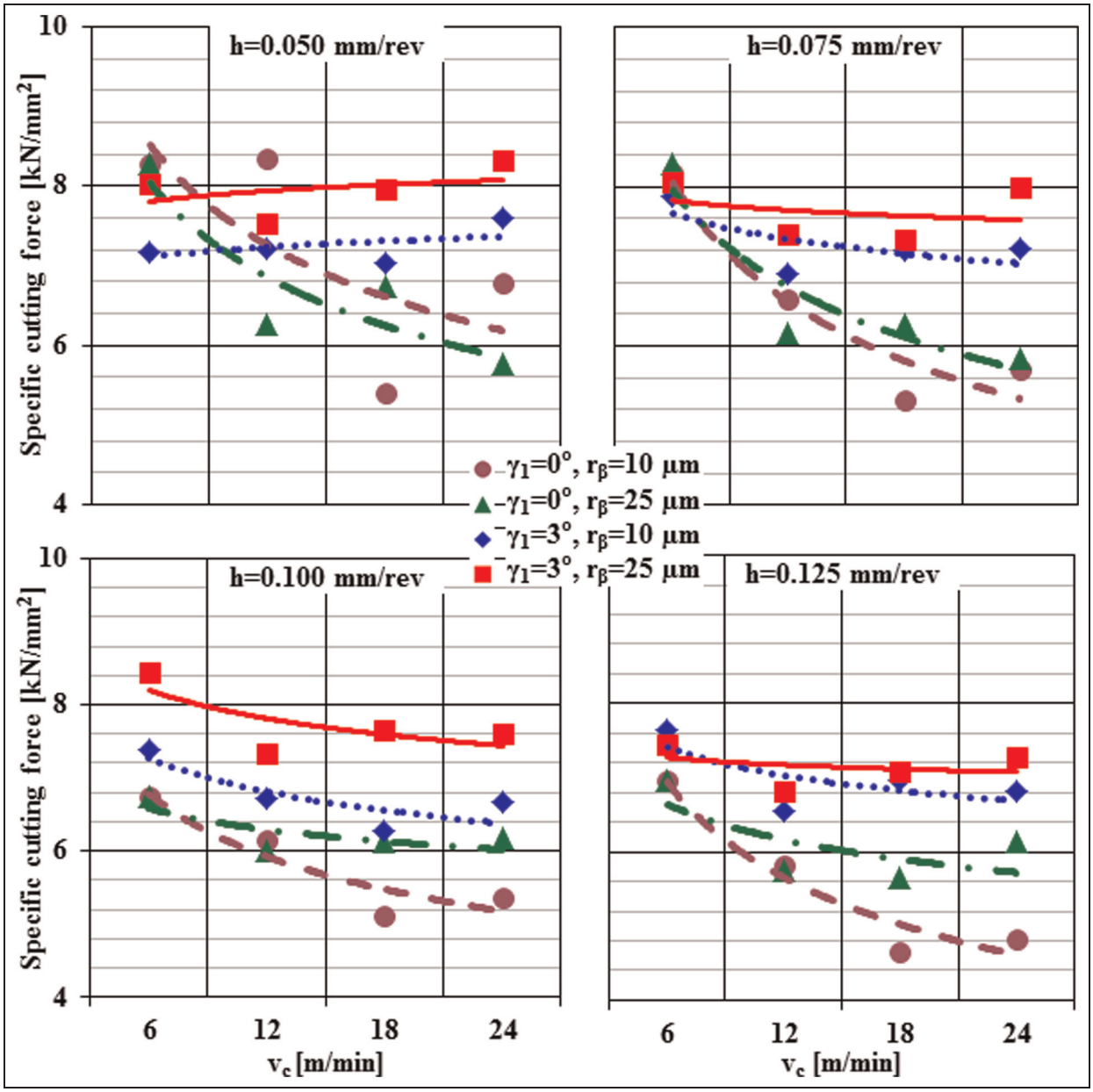

Figure 12. Measured specific cutting forces at lower and higher feeds (0.05–0.125 mm/rev).

Subbiah and Melkote.[30] First, forces in thrust and cutting directions are measured. Then, the friction angle (β) is found using the following equation

$$\beta = \gamma_1 + tan^{-1}\left(\frac{F_t}{F_c}\right) \tag{11}$$

From this equation, the shear angle is found as follows

$$\phi = \frac{\pi}{4} - \frac{\beta - \gamma_1}{2} \tag{12}$$

Then, various meaningful combinations of R and τ_y are created, and all of the combinations are subjected to calculation of $I = Rw/Q$ and $S = \tau_y w\gamma/Q$, which are the intercepts and slopes of the force graphs. When the ratio of (I/S) calculated this way is equal to the ratio (I/S) calculated from the force measurements, the calculation is ended and fracture toughness (R) and shear yield stress (τ_y) of the material, as well as the shear angle (φ), are found (see Table 2). These values are then used in the energy distribution formula to find the specific energies distributed to different sources of energy. Calculated energy distributions for plastic dissipation (shearing), friction dissipation and surface formation energy using this formulation are given in Figure 13. It should be noted that increasing surface formation energy should result in higher fracture toughness as it has been confirmed with the results presented here.

Analysis of friction coefficient

In determining the friction coefficient under dry machining conditions of nickel-based alloy, measured

Table 2. Influence of machining parameters on calculated fracture toughness (R) and the shear yield stress (τ_y) of the material.

		v_c (m/min)	R (MPa)	τ_y (MPa)	$I = Rw/Q$	$S = \tau_y w\gamma/Q$
$\gamma = 3°$	r_β = 10 μm	6	37.9	2247	51.9	7050
		12	15.3	784	58.4	6310
		18	12.9	840	48.6	6313
		24	66.6	794	259.2	6195
	r_β = 25 μm	6	62.0	2701	78.52	7096
		12	39.7	1819	56.8	6534
		18	54.9	2236	77.9	6557
		24	46.2	1719	71.7	6816
	r_β = 0	6	61.5	1655	84.4	5802
		6	61.1	1345	130.2	5811
$\gamma = 0°$	r_β = 10 μm	12	38.0	724	121.6	4968
		18	49.4	1040	75.1	4172
		24	57.5	918	91.2	4321
	r_β = 25 μm	12	31.6	1318	57.4	5322
		18	38.2	1114	84.9	5080
		24	117.2	1444	147.3	4563

cutting and thrust forces are utilized. Forces measured at two different rake angles and two different tool edge radii are shown in Figure 14. For zero rake angle cutting conditions, cutting forces and thrust forces increased linearly with the same slope between 0.025 and 0.1 mm/rev feed or uncut chip thickness. For a positive rake angle ($\gamma_1 = 3°$), thrust forces were lower; hence, the slope for thrust force trends was seen smaller indicating lower friction coefficient in those cutting conditions. Due to a possible size effect, thrust forces become greater than cutting forces when the feed (h) or uncut chip thickness is smaller than the tool edge radius (r_β).

Friction coefficient is calculated using two distinct methods: (1) mean friction coefficient method and (2) gradient-based friction coefficient method. Since the friction coefficient is quasi-steady along the friction surface, a constant mean value of the ratio of measured frictional force to cutting force could be used, which can be determined by equation (13) for the mean friction coefficient method. In gradient-based friction coefficient determination, experimental friction identification proposed by Albrecht[32] and improved by Arrazola and Meslin[33] has been utilized. Experimentally measured cutting (F_c) and thrust (F_t) forces for increasing feeds from 0.01 to 0.125 mm/rev were plotted against each other. The slope of the curve was calculated where μ is the friction coefficient and γ_1 is the rake angle. From the F_c–F_t plot, it is observed that the critical uncut chip thickness is higher than the cutting edge radius. The regions on the F_c–F_t plot can be correlated to the zones over the tool–chip contact area where high- to low-pressure contact areas exist. Equation (14) can be derived to find the coefficient of friction

$$\mu = \frac{F_c \sin\gamma_1 + F_t \cos\gamma_1}{F_c \cos\gamma_1 - F_t \sin\gamma_1} \tag{13}$$

$$\mu = tan\left[tan^{-1}\left(\frac{dF_t}{dF_c}\right) + \gamma_1\right] \tag{14}$$

Friction coefficients that are found using mean (average) friction coefficient method and gradient method have been compared with each other, as shown in Figure 15. The results indicated that average friction coefficient is higher when compared to friction coefficient obtained from gradient method. In addition, using gradient friction method, the effect of cutting speed on friction coefficient has been obtained, as shown in Figure 16.

Summary of the results and discussions

In orthogonal cutting tests, continuous but serrated chip formation is observed under the machining conditions considered in this study. At lower feeds, continuous chips with little or no serration were seen. Segmentation increased at higher feeds and cutting speeds similar to other observations reported in the literature.[16,25,27,28] Segmentation has been more dominantly affected by an increase in feed or uncut chip thickness.

The overall effects of machining conditions on the degree of segmentation indicate that increasing feed (h) results in higher degree of segmentation (D_s) when a positive rake angle ($\gamma_1 = 3°$) is used. Severe shearing ($\gamma_{sb} = 10$–30 mm/mm) occurs within the shear bands as a potential for fracture strain–initiated crack formation.

Measured specific cutting forces depict that positive rake angle and larger edge radius result in higher specific cutting forces. At higher cutting speeds, specific cutting force decreases due to thermal softening and strain softening at higher strain rates.

In machining nickel-based super alloy materials, work hardening behavior and the degree (or depth) of

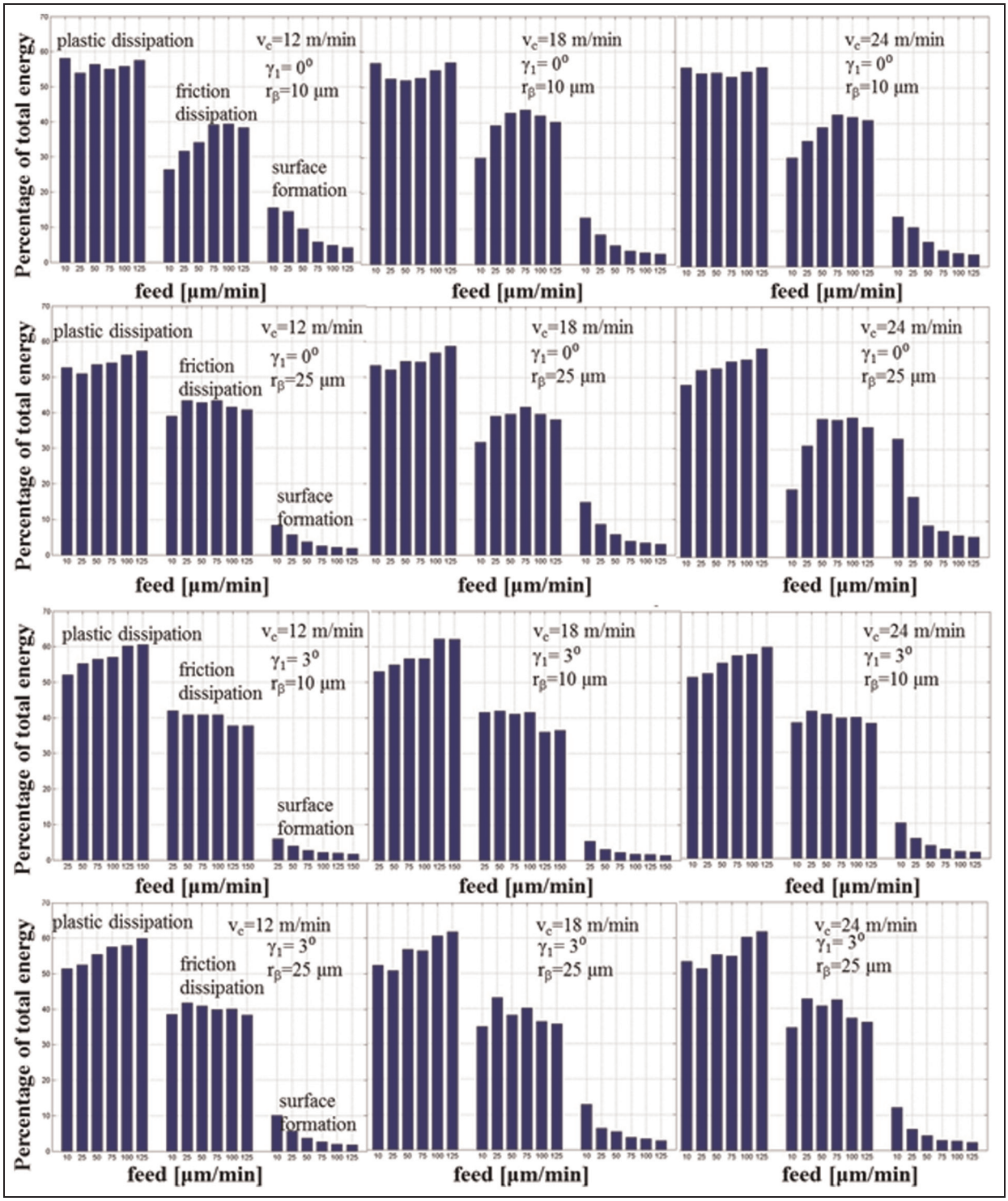

Figure 13. Calculated energy distributions for plastic dissipation (shearing), friction dissipation and surface formation energy.

work hardening were reported mainly as signs of severe plastic deformation. The energy dissipated through plastic deformation work has been found between 50% and 60% of the total machining energy. As feed increased, energy dissipation through plastic work increased. Energy dissipation through friction has been found to be ~40%, indicating a severe friction situation in machining of IN-100 nickel alloy. The energy spent for material separation and surface formation due to the fracture strength of the material has been found less than 10% of the total energy. But this component is substantially higher at low feeds (Figure 13).

Conclusion

In this study, mechanics of segmented chip formation and machinability of nickel-based super alloy IN-100, which is obtained from powder metallurgy and by

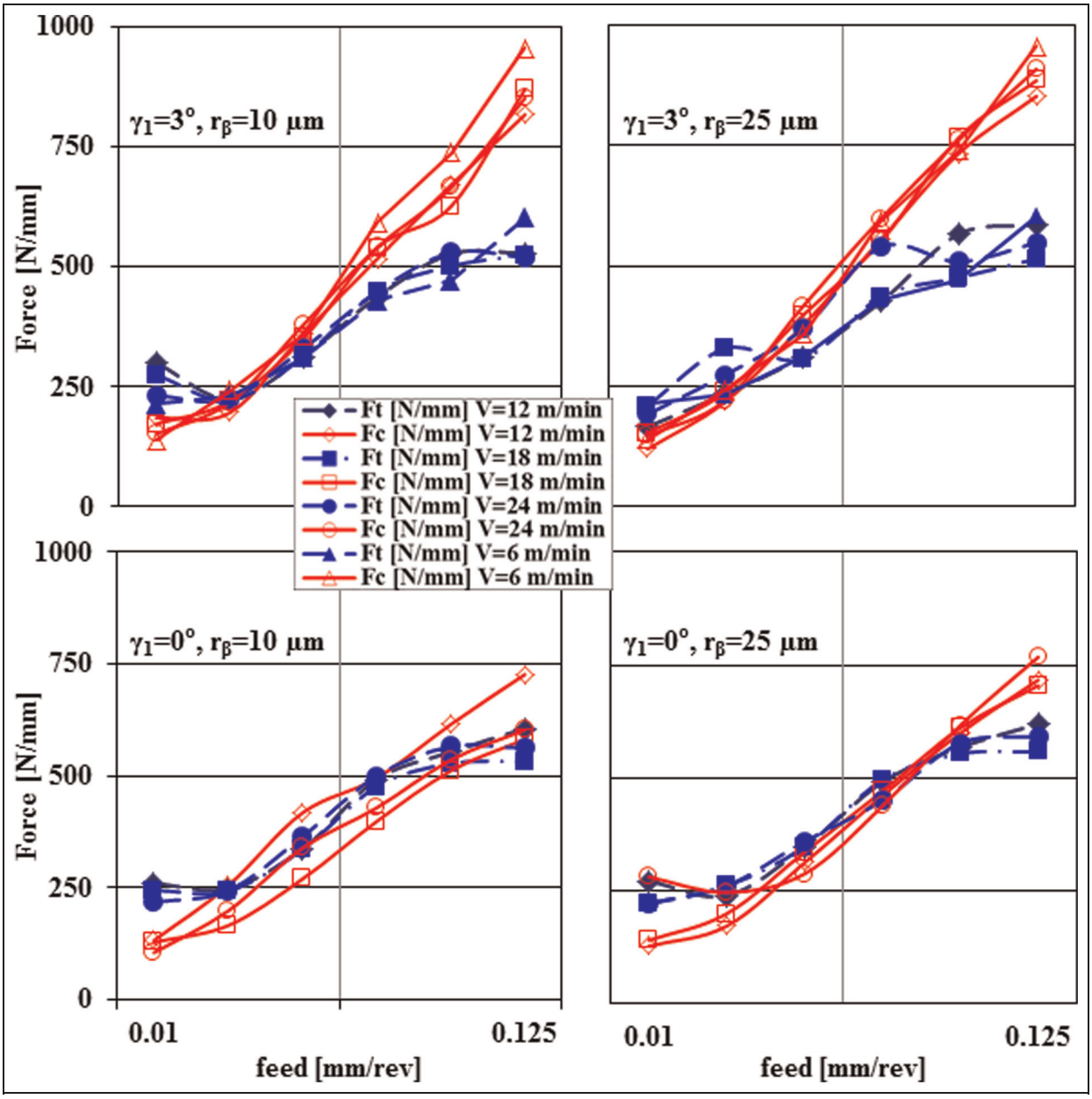

Figure 14. Experimentally measured cutting and thrust forces.

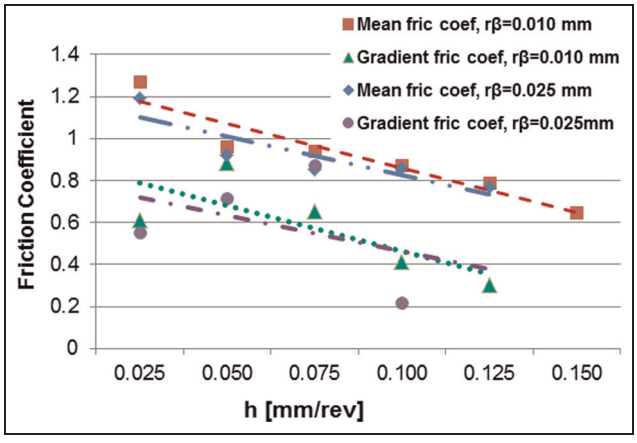

Figure 15. Comparison of friction coefficient obtained using mean friction coefficient method and gradient method for machining nickel-based alloy at v_c = 12 m/min.

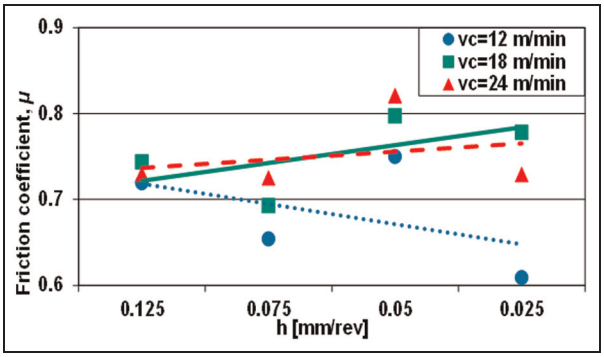

Figure 16. Friction coefficient identified using gradient method for γ_1 = 3° and r_β = 10 µm.

sintering, are investigated using orthogonal cutting tests. A range of machining parameters has been considered, and orthogonal cutting tests on IN-100 disks have been conducted using uncoated WC/Co cutting tools with two different rake angles and edge radii. Cutting forces are measured and effects of machining parameters on specific cutting forces are reported. Chip images are utilized in measuring and calculating chip formation angles, shear strain, and shear strain rate in the main shear zone and within the shear bands. Energy distributions calculated with regard to machining parameters reveal that friction dissipation and material separation are significant in machining of IN-100 nickel-based alloy. Furthermore, fracture toughness and shear yield stress have been calculated in each condition. It was found that material separation energy and fracture toughness of IN-100 material increase with decreasing cutting speed and feed but with increasing edge radius. These results also reveal some important aspects of nickel-based alloy machining, which may be useful for further investigations and modeling studies. Some specific conclusions on effects of machining parameters can be given as follows:

- Measured specific forces reveal that at higher cutting speeds, specific cutting force decreases due to thermal softening and material flow softening behavior at higher strain rates. Positive rake angle and larger edge radius resulted in higher specific cutting forces.
- Main shear angle is increased ~20% by increasing feed and increasing tool edge radius. While increasing cutting speed decreases the main shear angle more than 10%, increasing rake angle and edge radius decreases the main shear angle by ~10%.
- Main shear strain rate is largely affected by feed and cutting speed as expected.
- Segmented chip properties are also affected by machining conditions.
- Degree of segmentation is mainly affected by tool edge radius (decreases with increasing edge radius) and slightly affected by tool rake angle (increases with increasing rake angle).
- Shear strain in shear bands, which is a major indicator for secondary (or adiabatic) shearing, is affected by increasing feed and rake angle. However, increasing tool edge radius decreases shear band strain by about ~35%.
- Chip segment angle is also affected mainly by cutting speed (>20% decrease for 100% increase in cutting speed).
- Segmented shear angle increases with increasing feed and cutting speed by about ~10%−20%.

Acknowledgements

The authors acknowledge the assistance from Mr Michael Pandolfo and Mr Adam Miller during the experimental study and Mr Joshua Greenhaus for data analysis.

Declaration of conflicting interests

The authors declare that there is no conflict of interest.

Funding

This research was conducted through a contract agreement with United Technologies Research Center and partially supported by NSF grants CMMI-0758220 and CMMI-1130780.

References

1. Narutaki N, Yamane Y, Hayashi K, et al. High speed machining of Inconel 718 with ceramic tools. *CIRP Ann: Manuf Techn* 1993; 42(1): 103–106.
2. Rahman M, Seah WKH and Teo TT. The machinability of Inconel 718. *J Mater Process Tech* 1997; 63: 199–204.
3. Kitagawa T, Kubo A and Maekawa K. Temperature and wear of cutting tools in high-speed machining of Inconel 718 and Ti-6Al-6V-2Sn. *Wear* 1997; 202: 142–148.
4. Li L, He N, Wang M, et al. High speed cutting of Inconel 718 with coated carbide and ceramic inserts. *J Mater Process Tech* 2002; 129(1–3): 127–130.
5. Ezugwu EO, Bonney J and Yamane Y. An overview of the machinability of aeroengine alloys. *J Mater Process Tech* 2003; 135: 233–253.
6. Coelho RT, Silva LR, Braghini A Jr, et al. Some effects of cutting edge preparation and geometric modifications when turning Inconel 718™ at high cutting speeds. *J Mater Process Tech* 2004; 148(1): 147–153.
7. Arunachalam RM, Mannan MA and Spowage AC. Residual stress and surface roughness when facing age hardened Inconel 718 with CBN and ceramic cutting tools. *Int J Mach Tool Manu* 2004; 44: 879–887.
8. Arunachalam RM, Mannan MA and Spowage AC. Surface integrity when machining age hardened Inconel 718 with coated carbide cutting tools. *Int J Mach Tool Manu* 2004; 44: 1481–1491.
9. Sharman ARC, Hughes JJ and Ridgway K. Workpiece surface integrity and tool life issues when turning Inconel 718™ nickel based superalloy. *Mach Sci Technol* 2004; 8(3): 399–414.
10. Ezugwu EO. Key improvements in the machining of difficult-to-cut aerospace superalloys. *Int J Mach Tool Manu* 2005; 45(12–13): 1353–1367.
11. Sharman ARC, Hughes JJ and Ridgway K. An analysis of the residual stresses generated in Inconel 718™ when turning. *J Mater Process Tech* 2006; 173: 359–367.
12. Axinte DA, Andrews P, Li W, et al. Turning of advanced Ni based alloys obtained via powder metallurgy route. *CIRP Ann: Manuf Techn* 2006; 55(1): 117–120.
13. Pawade RS, Joshi SS, Brahmankar PK, et al. An investigation of cutting forces and surface damage in high-speed turning of Inconel 718. *J Mater Process Tech* 2007; 192–193: 159–146.
14. Joshi SV, Vizhian SP, Sridhar BR, et al. Parametric study of machining effect on residual stress and surface

roughness of nickel base super alloy UDIMET 720. *Adv Mat Res* 2008; 47–50: 13–16.
15. Pawade RS, Joshi SS and Brahmankar PK. Effect of machining parameters and cutting edge geometry on surface integrity of high-speed turned Inconel 718. *Int J Mach Tool Manu* 2008; 48: 15–28.
16. Pawade RS, Sonawane HA and Joshi SS. An analytical model to predict specific shear energy in high-speed turning of Inconel 718. *Int J Mach Tool Manu* 2009; 49: 979–990.
17. Zhang B, Mynors DJ, Mugarra A, et al. Representing the superplasticity of Inconel 718. *J Mater Process Tech* 2004; 153–154: 694–698.
18. Zou B, Chen M, Huang C, et al. Study on surface damages caused by turning NiCr20TiAl nickel-based alloy. *J Mater Process Tech* 2009; 209: 5802–5809.
19. Ranganath S, Guo C and Holt S. Experimental investigations into the carbide cracking phenomenon on Inconel 718 superalloy material. In: *Proceedings of ASME 2009 international manufacturing science and engineering conference*, West Lafayette, IN, 4–7 October 2009. New York: ASME.
20. Ranganath S, Guo C and Hegde P. A finite element modeling approach to predicting white layer formation in nickel superalloys. *CIRP Ann: Manuf Techn* 2009; 58: 77–80.
21. Wright PK and Chow JG. Deformation characteristics of nickel alloys during machining. *J Eng Mater Technol* 1982; 104: 85–90.
22. Komanduri R and Schroeder TA. On shear instability in machining a nickel iron base superalloy. *J Eng Ind: T ASME* 1986; 108: 93–100.
23. Sadat AB, Reddy MY and Wang BP. Plastic deformation analysis in machining of Inconel 718 nickel base superalloy using both experimental and numerical methods. *Int J Mech Sci* 1991; 33(10): 829–842.
24. Sinharoy S, Virro-Nic P and Milligan WW. Deformation and strength behavior of two nickel-base turbine disk alloys at 650 °C. *Metall Mater Trans A* 2001; 32: 2021–2032.
25. Gente A and Hoffmeister HW. Chip formation in machining Ti6Al4V at extremely high cutting speeds. *CIRP Ann: Manuf Techn* 2001; 50(1): 49–56.
26. Milligan WW, Orth EL, Schirra JJ, et al. Effects of microstructure on the high temperature constitutive behavior of IN100. In: Green KA, Pollock TM and Harada H (eds) *Superalloys*. Warrendale, PA: TMS, 2004, pp.331–339.
27. Cotterell M and Byrne G. Dynamics of chip formation during orthogonal cutting of titanium alloy Ti–6Al–4V. *CIRP Ann: Manuf Techn* 2008; 57(1): 93–96.
28. Fang N, Yang J and Liu N. Analytical predictive modeling of serrated chip formation in high speed machining of 7075-T6 aluminum alloy. In: *Proceedings of ASME 2004 international mechanical engineering congress and exposition*, Anaheim, CA, 13–19 November 2004. New York: ASME.
29. Atkins AG. Modelling metal cutting using modern ductile fracture mechanics: quantitative explanations for some longstanding problems. *Int J Mech Sci* 2003; 45: 373–396.
30. Subbiah S and Melkote SN. Evaluation of Atkins' model of ductile machining including the material separation component. *J Mater Process Tech* 2007; 182: 398–404.
31. Atkins AG. Toughness and cutting: a new way of simultaneously determining ductile fracture toughness and strength. *Eng Fract Mech* 2005; 72: 849–860.
32. Albrecht P. New developments in the theory of the metal-cutting process: part 1. *J Eng Ind: T ASME* 1960; 82(4): 348–358.
33. Arrazola PJ and Meslin F. A technique for the identification of friction at tool/chip interface during machining. In: *Proceedings of congress: 2nd ASIATRIB 2002 international conference*, Jeju Island, Korea, 21–24 October 2002.

Nomenclature

d_{ch}	chip segment length [mm]
D_s	degree of segmentation [-]
F_c	cutting force
F_t	thrust force
h	feed or uncut chip thickness [mm/min]
h_c	average thickness of the segmented chips [mm]
h_{c_max}	maximum thicknesses of the segmented chips [mm]
h_{c_min}	minimum thicknesses of the segmented chips [mm]
p_{ch}	pitch of the chip segments [mm]
p_{sb}	depth of segmentation [mm]
R	fracture toughness [MPa]
r_c	chip ratio [-]
r_β	edge radius [μm]
v_c	cutting speed [m/min]
V_{ch}	chip velocity [mm/min]
V_f	feed velocity (rate) [m/min]
V_s	shearing velocity [mm/min]
V_{seg}	velocity of the chip segmentation [mm/min]
w	width of cut [mm]
β	friction angle [degree]
γ	shear strain in the primary shear zone [mm/mm]
γ_{sb}	average shear strain in the shear bands [mm/mm]
γ_{seg}	average shear strain in segmented chip [mm/mm]
γ_1	rake angle [degree]
$\dot{\gamma}$	average strain rate [1/sec]
δ_{sb}	shear band thickness [mm]
μ	friction coefficient [-]
ϕ	shear angle [degree]
ϕ_{seg}	segmented shear angle [degree]
ρ_{seg}	chip segment angle [degree]
τ_y	shear yield stress [MPa]
τ_y	shear yield stress [MPa]